Impurity transport experiments and effects on MHD in the National Spherical Torus Experiment (NSTX)

2011 Nucl. Fusion 51 083047

(http://iopscience.iop.org/0029-5515/51/8/083047)

IOP Publishing and International Atomic Energy Agency Nuclear Fusion

Nucl. Fusion **51** (2011) 083047 (12pp) doi:10.1088/0029-5515/51/8/083047

Impurity transport experiments and effects on MHD in the National Spherical Torus Experiment (NSTX)

L. Delgado-Aparicio[1,a], D. Stutman[2], K. Tritz[2], F. Volpe[3], K.L. Wong[1], R. Bell[1], M. Finkenthal[2], E. Fredrickson[1], S.P. Gerhardt[1], S. Kaye[1], B. LeBlanc[1], J. Menard[2], S. Paul[1] and L. Roquemore[1]

[1] Princeton Plasma Physics Laboratory, Princeton, NJ 08543, USA
[2] The Johns Hopkins University, Department of Physics and Astronomy, Baltimore, MD, 21218, USA
[3] University of Wisconsin-Madison, Engineering Physics, Madison, WI 53706-1609, USA

E-mail: ldelgado@pppl.gov

Received 20 January 2011, accepted for publication 4 July 2011
Published 29 July 2011
Online at stacks.iop.org/NF/51/083047

Abstract
A first assessment of low-Z impurity transport in beam-heated NSTX H-modes has been performed using magnetic field and current scans at fixed q-profile as well as temperature scans at constant plasma density, current and toroidal field. Impurity diffusivity levels consistent with the neoclassical predictions have been found, whereas a reversal of the convective velocity at low fields indicates an anomalous effect to be at play at the gradient region. Studies on the impact of rotation in low-density H-modes have also shown that heavy and not fully stripped impurities with high Mach numbers can experience core diffusivities several times larger than that of the *'standard'* neoclassical transport for stationary plasmas, without the need of invoking the presence of long wavelength core electrostatic turbulence. As a result of a deliberate neon impurity injection we have also observed a correlation between the strength of the emitted radiation, the earlier appearance of tearing modes activity and an enhanced plasma cooling that resulted in enlarged magnetic islands.

(Some figures in this article are in colour only in the electronic version)

1. Introduction and motivation

Particle and impurity transport properties at low-aspect ratio remain important for extrapolation to future ST-based devices such as NSTX-Upgrade, NHTX and CTF [1] as well as to conventional aspect ratio schemes such as ITER. The National Spherical Torus eXperiment (NSTX) [2] is a low-aspect ratio tokamak ($A < 1.5$) that is able to sustain a high plasma β operating with $B_\phi \sim 0.35$–0.55 T, $I_p \sim 0.7$–1.1 MA and neutral beam injection (NBI) heating power up to 7.0 MW; the latter leads to core toroidal velocities of the order of 100–300 km s^{-1} and $\vec{E} \times \vec{B}$ shear rates up to $\sim$1 MHz. This shearing rate can be up to a factor of three to five greater than typical linear growth rates of long wavelength ion temperature-gradient modes, suppressing these instabilities partially if not completely. One of the ST predicted benefits is therefore the reduction of the anomalous ion transport, resulting in low core ($r/a < 0.7$) particle diffusivities in good agreement with the values predicted by neoclassical transport theory and important for the development of high confinement (H-mode) plasmas. This reduction in anomalous transport is generally attributed to the $\vec{E} \times \vec{B}$ shear stabilization of long wavelength microinstabilities [3], the stability of high-n ballooning modes [4] or a strong stabilizing factor of turbulent drift modes given by $\nabla\beta$ [5]. However, an unexpected effect of the strong toroidal rotation on impurity transport in NSTX is the possible increase in the impurity flux due to an enhanced collisional Pfirsch–Schlüter diffusivity and convective velocity associated with Coriolis and centrifugal forces. It has been found that heavy and not fully stripped impurities can experience a charge-dependent diffusion coefficient several times larger than that of the charge-independent neoclassical transport for stationary plasmas, without the need of invoking the presence of long wavelength electrostatic turbulence. A first experimental assessment of this core impurity transport effect in a strongly rotating H-mode resulted in core impurity

[a] Presently at the Massachusetts Institute of Technology (MIT), Plasma Science Fusion Center (PSFC, Cambridge, MA, 02139, USA).

diffusivities higher than that of standard neoclassical values and in agreement with a Mach-corrected Pfirsch–Schlüter diffusivity. As a result of a deliberate neon impurity injection we have also observed a correlation between the strength of the emitted radiation, the earlier appearance of tearing modes (TMs) activity and an enhanced plasma cooling that resulted in enlarged magnetic islands. Assessing the impact of impurity radiation as a driving mechanism for TM activity is important for the development of any magnetically confined plasma scheme. This paper is organized as follows: a brief description of the main diagnostic used and a review of the field and temperature scans of impurity transport in NBI heated H-mode plasmas is outlined in sections 2 and 3; in section 4 we discuss the relationship between the enhanced particle fluxes and toroidal rotation, while the correlation between the strength of the emitted radiation, the plasma cooling and the early appearance of TMs activity is discussed in section 5.

2. Main diagnostic used for impurity transport and MHD studies

The tangential (scintillator based) multi-energy (ME) soft x-ray (SXR) array [6–11] has been the main diagnostic used in NSTX for describing the effects of impurity transport and MHD in the background plasma. This diagnostic had three identical groups of overlapping sightlines that view the same plasma volume using beryllium foils of different thicknesses; the specific selection of these SXR filters was such that their low ($E_{C,10\%} \sim 786$ eV), medium ($E_{C,10\%} \sim 1700$ eV) and high ($E_{C,10\%} \sim 2500$ eV) cut-off energies (for 10% of SXR transmission) are also approximately equal to $1 \times \langle T_e \rangle_l$, $2 \times \langle T_e \rangle_l$ and $3 \times \langle T_e \rangle_l$, where $\langle T_e \rangle_l$ is the line-average electron temperature in typical NSTX discharges. Although this system was originally envisioned for fast electron temperature measurements and MHD studies, it is also filtered for energy bands covering the entire neon spectrum emitted from NSTX. The impurity transport experiments to be described in the next sections used a transient neon puff injected from an outboard mid-plane port as an impurity particle source with a strong spectral signature in the SXR range 0.1–2.0 keV (see [9, 10]). These SXR metallic foils are thus used to discriminate between the 0.9–1.3 keV line emission (e.g. from H- and He-like neon ions) mostly dominant in the peripheral plasma, and the enhanced continuum emission (from fully stripped neon ions) primarily from the inner plasma; additional information on this filtering technique, the view of choice in NSTX and a variety of applications in which the ME-SXR array has been used (e.g. fast electron temperature measurements, particle transport and resistive wall mode studies, to mentioned just a few) can be found in [6–11] and references therein.

3. Field and temperature scans of impurity transport in NSTX

The first impurity transport experiments performed in beam-heated NSTX H-modes were done by simultaneously varying the external toroidal field (B_ϕ) and the plasma current (I_p) to observe transport and confinement effects at fixed $q_{95} \sim B_\phi/I_p$. The neon injection and resultant impurity transport measurements were performed under two different conditions: the lower-field ($I_p = 1.0$ MA–$B_\phi = 0.45$ T) and higher-field ($I_p = 1.2$ MA–$B_\phi = 0.55$ T) plasmas; see [9, 10] for details on these experiments. These plasmas were double-null diverted (DND), with average elongation (κ) and triangularity (δ) of the order of 2.25 and 0.6, respectively. Despite the differences in I_p and B_ϕ, the plasma shape and q-profile of the two discharges were well matched largely due to the real-time control of the plasma boundary [12]. Operation at moderate plasma β with a central safety factor $q > 1$, allows the avoidance of sawteeth, internal reconnection events and large ELMs, which could affect the magnitude and interpretation of the measured impurity transport coefficients. These H-mode discharges were also characterized by $T_i/T_e > 1$ throughout the NSTX cross section, despite the fact that only about 30–40% of the NBI power was computed to heat the ions ($E_{NBI} \sim 90\,\text{keV} \gg T_e$). Figures 1(*a*) and (*b*) show the 2 ms time-averaged experimental (low-energy) neon SXR emissivities for both the low- and high-field cases. A comparison between the edge and core signals in figure 1 indicates that the impurity build-up and its subsequent penetration to the core change substantially when both the plasma current and the toroidal field are increased [10]. The time histories of the neon emissivity profiles after the injection were modelled using the one-dimensional (radial) and time-dependent multiple ionization stage transport (MIST) code [13] (see figures 1(*c*) and (*d*)). This simulation incorporates electron ionization, excitation and recombination processes for calculations of sinks and sources as well as ion particle transport coefficients. MIST was used to model the evolution of neon charge states using the experimental time histories of $n_e(R, t)$ and $T_e(R, t)$ and assuming external profiles of charge-independent neon diffusivity and convective velocity (see [10] and references therein). The MIST transport parameters were adjusted until a self-consistent solution matched both the neon emissivity computed through MIST with the ME-SXR emissivity reconstructions and the total radiated power with bolometer measurements. The neon-recycling coefficient used was $\lesssim$1.0 and the constraints for particle sources were imposed using the radiated power measured by a tangential midplane bolometer array.

The neon diffusion coefficients inferred from the MIST modelling are presented in figure 2(*a*) and decrease from a several $m^2\,s^{-1}$ in the outboard plasma to a fraction of $m^2\,s^{-1}$ inside r/a <0.8. The band of values represents the range of transport coefficients that reproduce the measured SXR emissivities in two distinct spectral ranges within 10% or less; details on how the uncertainties related to these profiles have been assessed can be found in [8, 10, 14]. It is interesting to note that for the gradient region ($R \gtrsim 137$ cm, $\rho \gtrsim 0.8$) the neon MIST diffusivity is greater than $1\,m^2\,s^{-1}$ and increasing strongly with radius. Concerning B-scaling, the experiment shows within error bars the $1/B^2$ neoclassical dependence inside $r/a < 0.7 - 0.8$ (see figure 2(*b*)); this is an additional indication, together with the similarity of the experimental and neoclassical diffusion profiles, that the neon diffusion in the plasma core is in the neoclassical range. Additionally, the MIST and NCLASS [15] diffusivities in the outer plasma $r/a \gtrsim 0.8$ are also increasing with radius to a few $m^2\,s^{-1}$ possibly due to the strong collisionality and rapidly increasing q^2 dependence of the collisional Pfirsch–Schlüter diffusivity. The neon convective velocities inferred

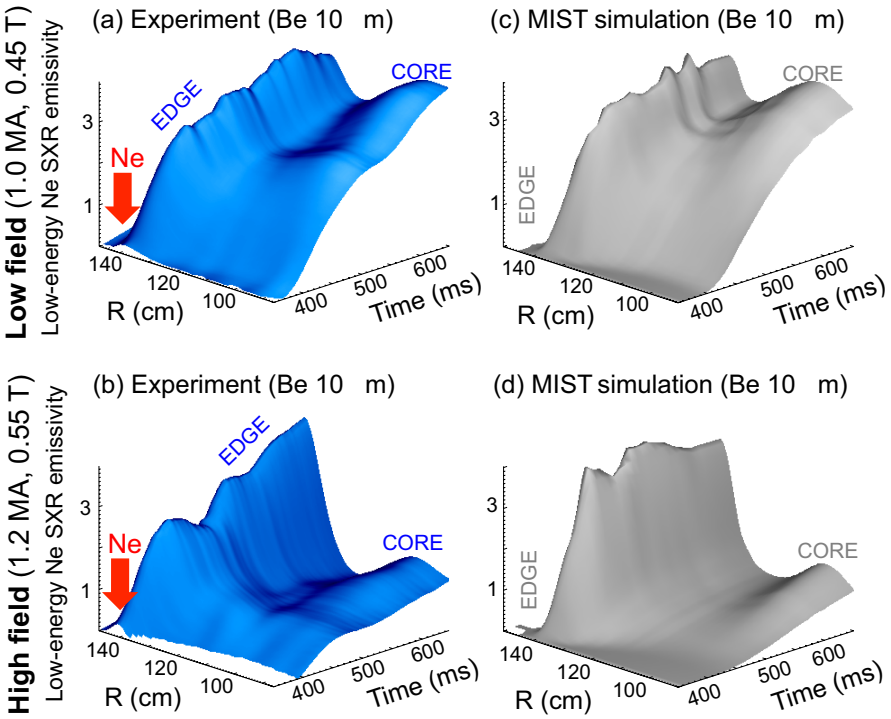

Figure 1. Experimental and MIST simulated neon SXR emissivity profiles filtered with a (low-energy) Be 10 μm foil for low-field (1.0 MA–0.45 T) and high-field (1.2 MA–0.55 T) H-mode plasmas. Good agreement between measurements and simulations have been found showing how neon injected at $t = 350$ ms transports and accumulates at different rates in the low- and high-field cases.

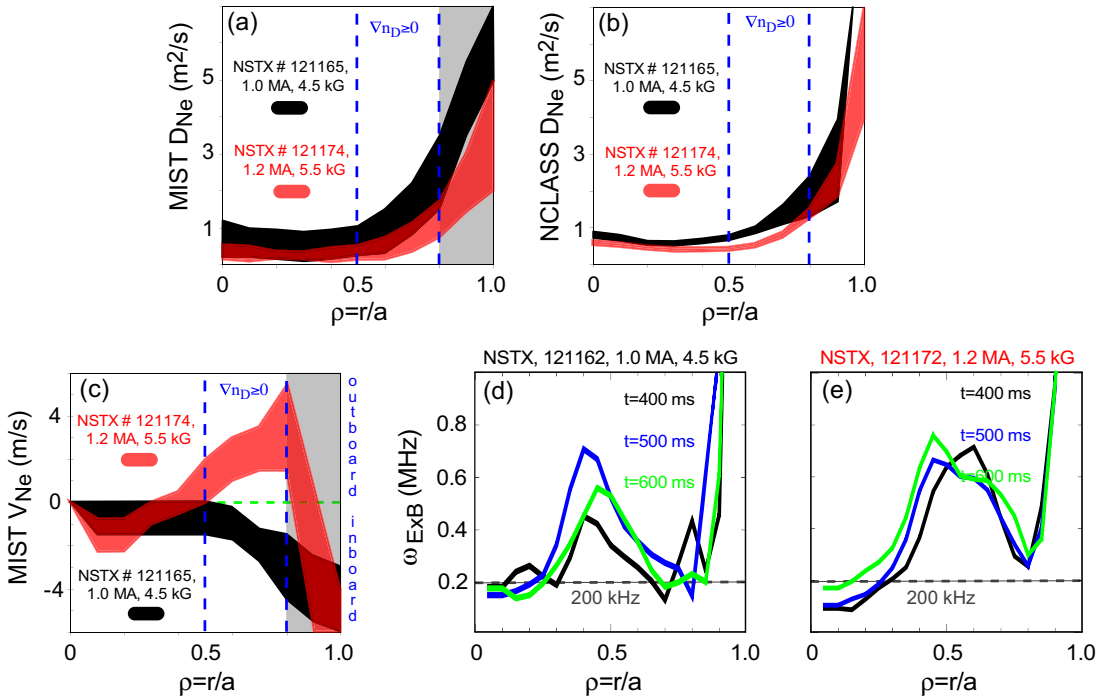

Figure 2. Neon diffusivity calculated by (*a*) MIST and (*b*) NCLASS codes. The MIST convective velocity and NCLASS $\vec{E} \times \vec{B}$ shear rates for the low- and high-field H-mode are depicted in (*c*), (*d*) and (*e*), respectively. The vertical dotted lines indicate the region where the pinch velocity is reported to have changed even though $\nabla n_D \geqslant 0$ in both cases.

from the MIST modelling are presented in figure 2(*c*). For the high-field and high-current case an outward (positive) convective velocity of a few m s^{-1} in the region $r/a > 0.4$ is needed to model the low level of impurity accumulation inside the NSTX mid-radius and the hollow nature of the SXR emissivity profiles. However, to model the peaking of neon emissivity for the low-field H-mode, one needs an inward pinch velocity. In summary, impurity diffusivity levels

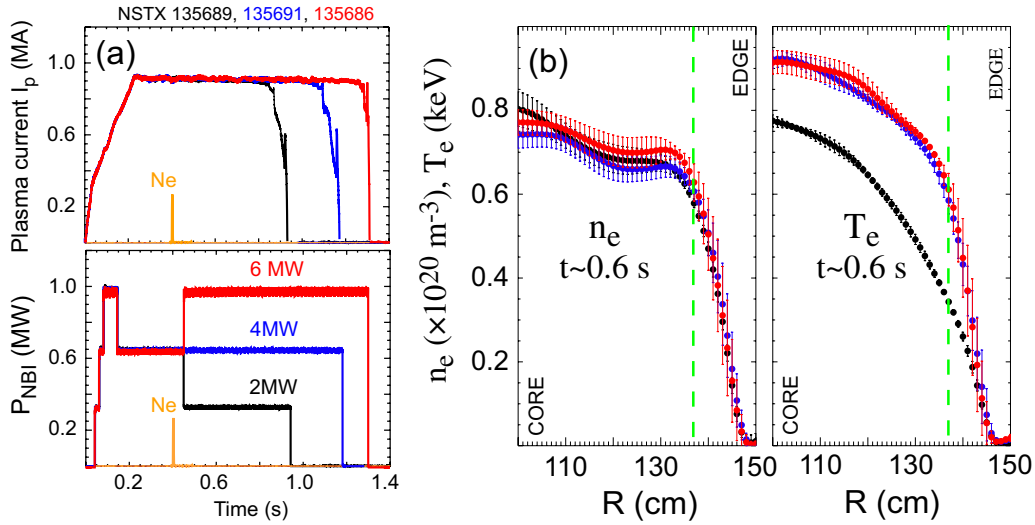

Figure 3. $\nu^* \propto T^{-2}$-scan of NBI power at constant plasma current, density and toroidal field. The vertical dotted lines indicate the location where the maximum change in ν^* was observed.

consistent with neoclassical predictions have been found, whereas a reversal of the convective velocity in the low-field case indicates some anomalous effect to be at play at the gradient region. Tentatively, we attribute the high density of neon and the needed (anomalous) negative pinch velocity to the incomplete shear suppression at low fields (compare wider $\vec{E} \times \vec{B}$ shear rates for the high-field H-mode shown in figure 2(*e*)) and the presence of drift-wave electrostatic ITG/TEM modes at the outer plasma [17–21]; experimental findings of neoclassical diffusivity with anomalous convective velocity have also been reported in high-aspect ratio tokamaks (see [18] and references therein).

The anomaly at the gradient region observed for the lower-field H-mode case was further explored with a temperature-scan of impurity transport, but this time using distinct NBI heated plasmas with plasma density, current and toroidal field held constant (see figure 3). The high-power (4 and 6 MW) NBI H-modes have as much as twice the electron temperatures in the gradient region relative to that at low power, with an associated normalized collisionality $\nu^*[\nu^* = \nu/(v_{th}/Rq) \propto n_D q/T^2]$ varying up to a factor of four with nearly identical density profiles (see figure 3(*b*): the region of interest is at $R \sim 130$–142 cm and/or $r/a \sim 0.6$–0.8). Low- and high-energy emissivity reconstructions for the 2 and 6 MW cases are shown for comparison in figure 4. The low-energy emissivities (see top panel) sensitive to line radiation from He- and H-like neon ions indicate that the core emissivity decreases with NBI power while increasing at mid-radius and the gradient region. However, the high-energy emissivity (see the bottom panel) sensitive to the enhancement of the continuum from fully stripped neon, suggests that both the core and mid-radius signals increases with NBI power indicating a possible change in the impurity transport characteristics at the gradient region where ν^* varied a factor of four. Results from MIST transport simulations (see figure 5) indicate, however, that a factor of two increases in electron temperature could be solely responsible for modifying the neon charge state distribution that will explain the differences in the observed SXR emissivity (see figures 5(*b*) and (*c*): the region of interest is $0.5 < r/a < 0.9$). Different charge state distributions as a consequence of different background plasma parameters in the gradient region (e.g. due to differences in $T_e(R, t)$ profiles) have to be taken into account when modelling the impurity transport at low fields, and may be solely responsible for the change in SXR emissivity. In summary, the tentative change in impurity transport at the gradient region for the low- versus high-power low-field H-modes can be explained within the grounds of atomic physics without the need of changing the underlying diffusive and convective transport properties; the anomalous pinch velocity at the gradient region reported above (for the low-field H-modes) appear thus to be unaffected in this new set of experiments.

4. Enhanced Pfirsch–Schlüter impurity flux in the core of a rotating plasma

The main motivation for performing this study is to find a reliable model to characterize the transport properties of low-density H-mode scenarios with high toroidal velocities in which the *'standard'* neoclassical theory (e.g. NCLASS [15]) derived for 'subsonic' Mach numbers may no longer be applicable [16]. Examples of NSTX-related scenarios and/or calculations of flux-surface average quantities in which a high Mach number formalism may be applicable are for instance:

(i) H-mode plasmas obtained using lithium coatings for density pump-out can have lower densities that present H-modes and thus possibly higher core toroidal velocities for the same toroidal momentum input; deuterium Mach numbers of the order of one [$M_D \lesssim \mathcal{O}(1)$] can be obtained and their description using standard neoclassical theory will no longer be adequate.

(ii) The use of a second tangential neutral beam is being considered for the next NSTX-Upgrade facility; although the second NBI 'box' was originally conceived for modifying and/or tailoring the current density profile (e.g. bootstrap current), it will also provide additional momentum to the outward low temperature plasma thus increasing the local Mach number.

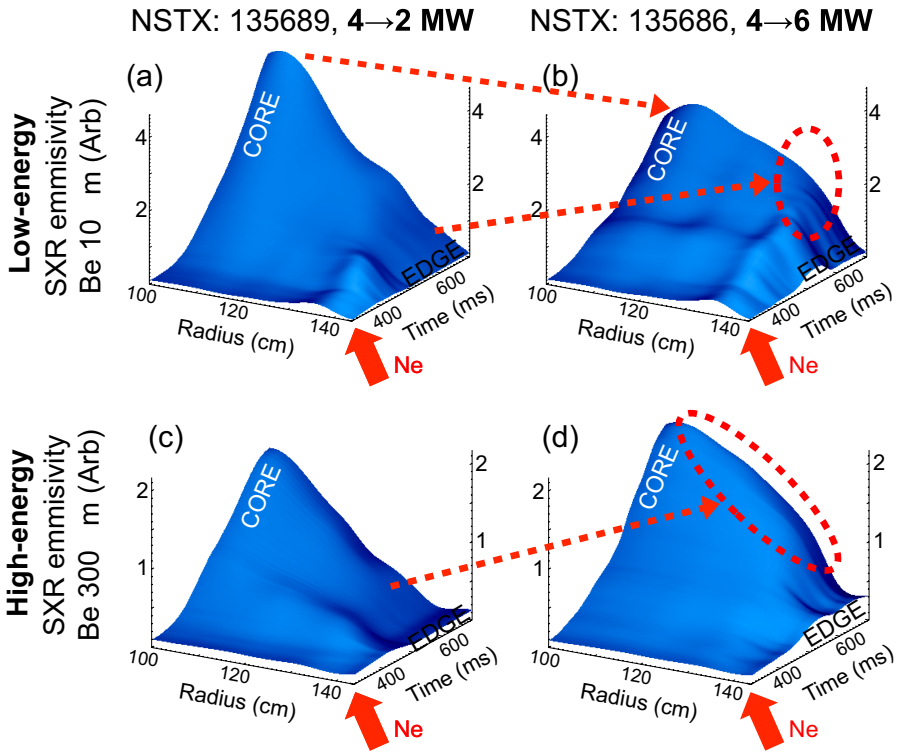

Figure 4. Low- and high-energy SXR emissivities for the 2 and 6 MW cases.

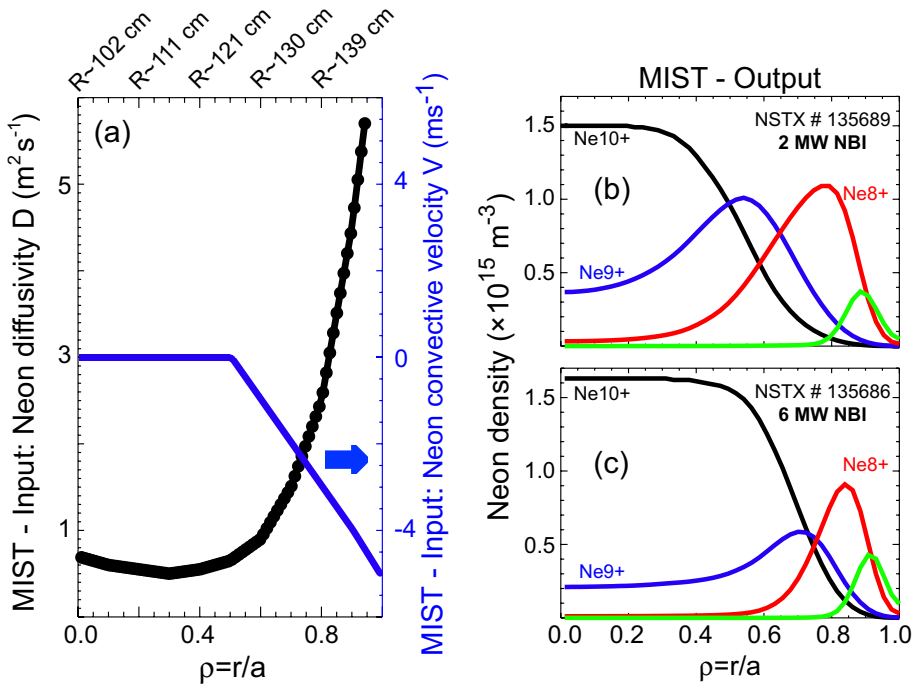

Figure 5. MIST diffusion and convective transport coefficients together with the different density of neon charge states calculated for H-mode plasmas heated with 2 and 6 MW of NBI power.

(iii) Poloidal asymmetries in impurity density resultant from high Mach numbers can impact the assessment of its flux-surface-average and hence the resultant $\langle Z_{\rm eff}\rangle$; the latter is used in the calculation of the neoclassical conductivity and the interpretation of non-inductive and inductive current fractions.

4.1. Standard charge-independent neoclassical scaling versus the charge-dependent enhanced Pfirsch–Schlüter impurity diffusivity in a rotating plasma frame

The standard collisional Pfirsch–Schlüter neoclasical impurity diffusivity in a non-rotating plasma frame of reference can be

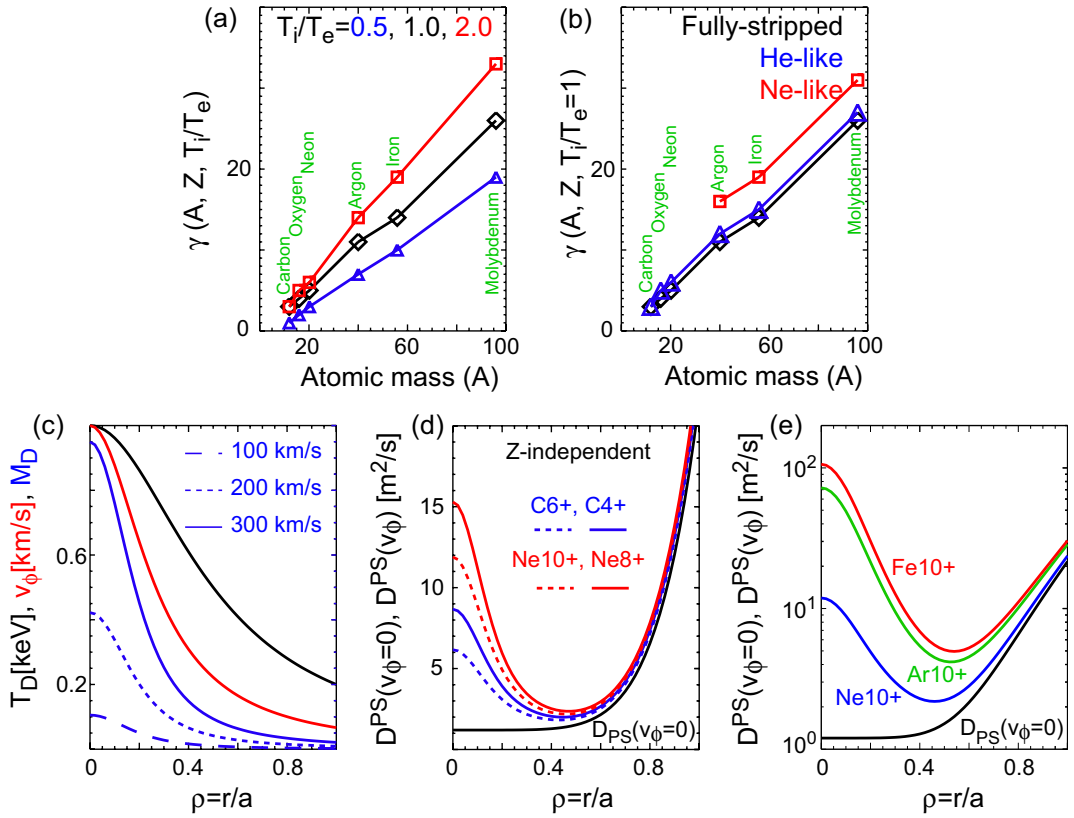

Figure 6. (*a*) Temperature-, (*b*) charge state and mass dependence of γ. Synthetic profiles for ion temperature, normalized toroidal velocity and the resultant Mach numbers are indicated in (*c*), while with the Pfirsch–Schlüter diffusivities for fully stripped and He-like carbon and neon are depicted in (*d*). Enhanced diffusivities for fully stripped neon and neon-like argon and iron are shown in (*e*).

expressed as in equation (1). For the large-aspect ratio circular approximation and in the limit of $K_Z^{PS} \to 1$ [10], the product of the first two terms in the right-hand side of equation (1) reduces to the neoclassical toroidal $2q^2/B_{\phi,0}^2$ enhancement over the cylindrical approximation and is thus charge independent (see equation (2)):

$$D_Z^{PS} \approx \frac{\langle RB_\phi\rangle^2}{(\partial\psi/\partial r)^2}\left(\langle B^{-2}\rangle - \langle B^2\rangle^{-1}\right) K_Z^{PS}\frac{m_Z k_B T_Z \nu_{Z,D}}{Z^2 e^2} \quad (1)$$

$$\propto \rho_Z^2 \nu_{Z,D} q^2$$

$$= \frac{k_B T_Z/m_Z}{Z^2 e^2 B^2/m_Z^2}\cdot\frac{e^4 Z^2 n_D \ln\Lambda_{Z,D}}{m_Z m_D^{-1/2} T_i^{3/2}} \propto \frac{1}{B^2}\frac{n_D}{T_i^{1/2}} q^2. \quad (2)$$

The effects of toroidal rotation on impurity transport were first considered by Wong *et al*, Romanelli *et al* and Wesson (see [22–26] and references therein); the representation used described impurity particle orbits in fluid-like models thus obtaining rotation-enhanced Pfirsch–Schlüter diffusion coefficients (in the high-aspect ratio approximation) that included Coriolis and centrifugal forces together with an approximate form of the radial dependence of impurity density. Although their analytical expressions appear to be qualitatively different, it is now possible to rewrite them using the same functional form as described below (see equations (3)–(6)). The few assumptions made considered a deuterium plasma ($Z_i \approx 1$ and $m_i = m_D \approx 2m_p$), a trace impurity with charge Z, mass $A \approx m_I/m_p$ and an impurity temperature $T_I \approx T_i$; γ_Z^A is a dimensionless function that depends strictly on the impurity mass, charge and the T_i/T_e ratio while M_D is the deuterium Mach number. In a stationary plasma, these models reduce to the charge-independent Pfirsch–Schlüter impurity diffusivity discussed in equation (2). It is worth noting that this rotation-enhanced particle diffusivity (and convective velocity, not discussed here) depends on even powers of 'v_ϕ' and thus independent of the direction of plasma rotation, explaining some of the impurity injection results from the Princeton Large Torus using co- and counter-propagating beams [27]:

$$D_{Z,v_\phi}^{PS}(\gamma_Z^A, M_D, R) = D_{Z,v_\phi\to 0}^{PS}\left(1+\gamma_Z^A\cdot M_D^2\cdot\frac{R_0^2}{R^2}\right)^2, \quad (3)$$

$$\frac{n_Z}{n_{Z,0}} \approx \exp\left\{\gamma_Z^A\cdot M_D^2\left(1-\frac{R_0^2}{R^2}\right)\right\}, \quad (4)$$

$$\gamma_Z^A = \frac{A}{2}\left\{1-\frac{2Z}{A}\left(\frac{T_e}{T_e+T_i}\right)\right\}, \quad (5)$$

$$M_D^2(v_\phi, T_D) = v_\phi^2/v_{th,D}^2 \approx 1.05\times 10^{-5} v_\phi^2 \quad (\mathrm{km\,s^{-1}})/T_D(\mathrm{keV}) \quad (6)$$

The mass-, charge- and temperature-dependence of γ_Z^A is shown in figures 6(*a*) and (*b*) for different impurities from carbon to molybdenum. The effect of having a higher T_i/T_e ratio is equivalent to 'reduce' the impurity charge which in turn will result in increasing γ_Z^A; impurities which are not fully stripped (e.g. neon-like argon and iron) may have ~20% higher γ_Z^As which can also translate into higher core diffusivities. Synthetic data describing peaked ion-temperatures of 1.0 keV and a normalized toroidal velocity have been generated using

Lorentzian profiles; the resultant deuterium Mach numbers have been computed for the cases of core velocities of 100, 200 and 300 km s^{-1} and are shown in figure 6(*c*). An intermediate case of a modified Pfirsch–Schlüter diffusivities (using a core $v_\phi \sim 200\,\mathrm{km\,s^{-1}}$) for fully stripped and He-like carbon and neon are compared with the 'non-rotating' counterpart and depicted in figure 6(*d*). This comparison shows good agreement at the outer radii since the Mach number is low ($M_\mathrm{D} < 0.1$) but a rather large discrepancy at the core where $M_\mathrm{D} > 0.1$. The change in impurity diffusivity is even more dramatic if one considers the mass dependence at a constant impurity charge as shown in figure 6(*e*); the fully stripped neon and the neon-like argon and iron can have an enhanced diffusivity as much as one to two orders of magnitude higher than its 'non-rotating' neoclassical counterpart. In summary, the collisional charge-dependent Pfirsch–Schlüter neoclassical diffusivity for heavy impurities can be one to two orders of magnitude higher in a deuterium rotating plasma than in a stationary one, without the need of invoking the presence of long wavelength electrostatic turbulence. Although the impurity peaking factors do not change from the standard neoclassical description, the enhanced diffusivity and convective velocity can account for an enhancement over the conventional Pfirsch–Schlüter impurity fluxes that could result in stronger and possibly unexpected radiated powers. A detailed paper on this topic will be the subject of a future study.

4.2. The first experimental results at high Mach numbers

The motivation for performing impurity transport experiments using impurity-embedded pellets was to assess the time-dependent characteristics of the transport matrix by probing the time evolving effects of quantities such as toroidal rotation. The scenario which is of noticeable interest is the low-density H-modes in which toroidal velocities of up to 300 km s^{-1} and $M_\mathrm{D} \sim 0.8$–0.9 have been obtained. A first assessment of core impurity transport in the strongly rotating early H-mode phase was performed using a 0.5 mg ablation resistant vitreous carbon pellet [28] deposited deep in the plasma in comparison with that of the outer perturbation introduced by the gas injection. The carbon pellet injection technique was envisioned and used for controlled T_e perturbations needed for perturbative studies of electron transport in NSTX [28]. The evolution of the impurity density profile (δn_Z in $\Delta t \sim 50$ ms) is much slower than that of temperature perturbation (δT_e in $\Delta t \sim 1$ ms), and thus estimates of carbon diffusivity can be obtained using the 1D-radial transport code MIST (see figure 7) coupled with the carbon density time history profiles available from the charge exchange recombination spectroscopy (CHERS) diagnostic (see [28]). While the carbon diffusivity in the outward plasma ($r/a > 0.6$) seems to agree well with neoclassical ordering of 1 m^2 s^{-1} such as the one depicted in figure 2, the core transport ($\sim$4–9 m^2 s^{-1}) appears to be enhanced above the neoclassical values reaching several times the NCLASS predictions. The core toroidal velocity was 200 km s^{-1} and $M_\mathrm{D} \sim 0.4$ so in the case of fully stripped carbon, the enhancement over the standard neoclassical value should be a factor of five, well within the error bars of the core carbon diffusivity measurement. The effect of plasma rotation on core impurity transport has therefore been considered as the first 'non-turbulent' candidate to explain this 'enhanced' neoclassical transport.

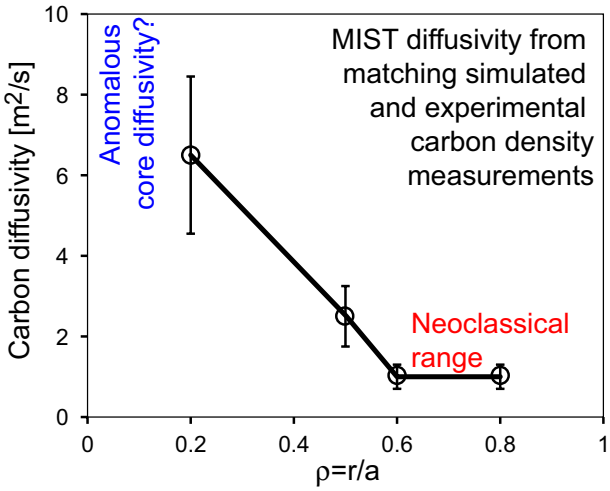

Figure 7. MIST carbon diffusion for the early phase of an NSTX H-mode. Figure adapted from [28].

5. Effects on MHD: impact on TM onset and stability

This study was motivated by the early appearance of TM activity in neon-seeded H-modes in both the field and current scan (see figure 3 in [10]) as well as on the temperature-scan experiments described above. By the end of the current flattop for the discharges shown in figure 3 of this paper, we observed the development of a $m/n = 2/1$ TM as depicted also in figure 8 (w/o early neon injection); the appearance of the TM activity $\sim$100 ms earlier in the neon-seeded H-mode (see data in blue in figure 8(*a*)) seems to be related to the ($\sim$220 kW) enhanced radiated power from neon continuum and line emission since the plasma density and temperatures profiles are similar before the two TM onsets. When the TM develops in the neon-free H-mode, the temperature-dependent high-energy SXR emissivity (shown in figure 8(*b*)) shows a sudden drop at mid-radius possibly indicating the island location where the plasma cooling associated with the temperature flattening takes place. The low-energy emissivity, on the other hand, shows a non-varying value at mid-radius but an asymmetric 'inward' growth of the region of 'flat' emissivity for $r/a < 0.5$ ($R < 125$ cm). The MPTS density profiles for the first 50 ms from the mode onset (not shown here) describe a flat electron density at mid-radius with a small density increase at the core, which translates into the small increase in the low-energy core SXR emissivity also shown in figure 8(*c*). The use of the emissivity profiles from the multi-energy SXR diagnostic in NSTX allows us for the first time to simultaneously image the location at mid-radius where the island growth and plasma cooling took place.

The well-known neoclassical tearing modes (NTMs) are a magnetic island driven by a helical perturbation that result in a 'hole' in the bootstrap current. These MHD perturbations from equilibrium can grow unstable according to resistive and transport constraints and can lead to confinement degradation, potential mode-locking and disruptions. Recent observations of exponentially growing TMs in ASDEX-UPGRADE [29], RTP [30–34] and TEXTOR [35] tokamaks support the idea of having an additional driving mechanism proportional to

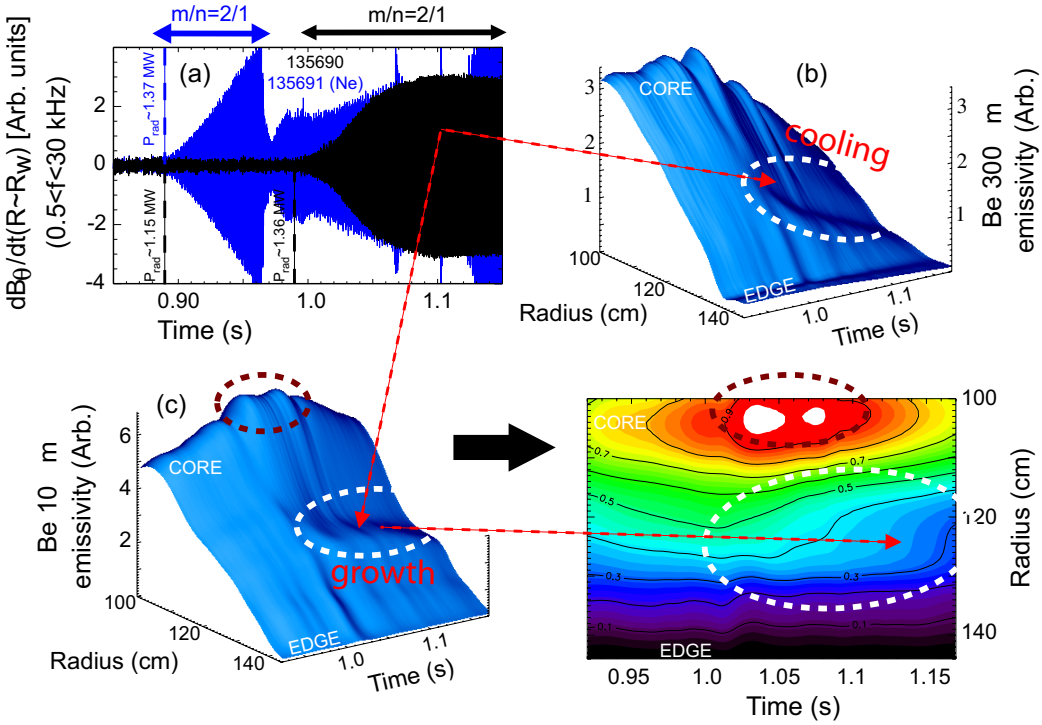

Figure 8. (*a*) Mirnov ($\mathrm{d}B/\mathrm{d}t$) data indicating the presence of an MHD mode in H-mode plasmas with and without neon seeding. Both the cooling and growth of the island at mid-radius is observed using the (*b*) high- and (*c*) and (*d*) low-energy SXR emission.

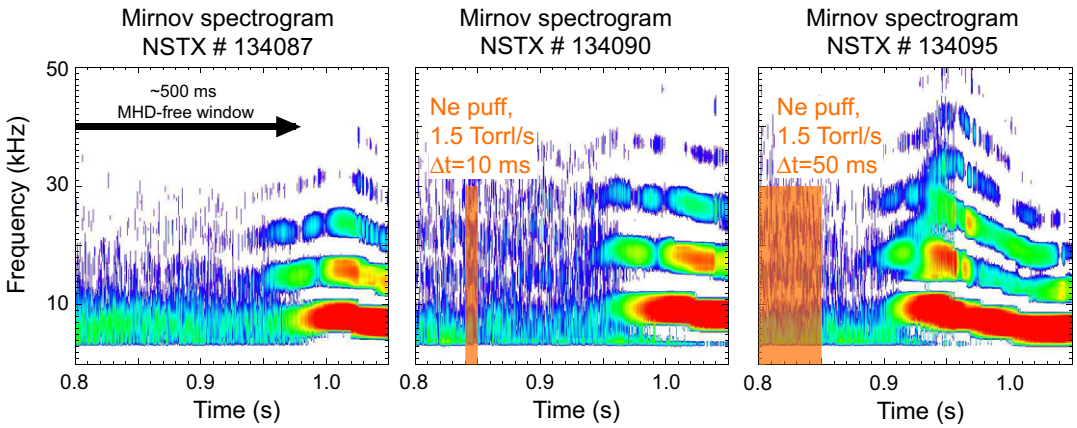

Figure 9. Mirnov spectrograms indicating the effect of the 10–50 ms Ne-puffs anticipate the MHD mode onset by 20–80 ms. The shaded regions indicate the time intervals during which neon is puffed.

the changes in Z_{eff} and the radiated power density in the centre of the island, which can be modelled using the extended Rutherford formalism [36–38] used to describe NTMs. A systematic study of the role of impurities affecting the TM onset and evolution by providing an enhanced radiation and associated cooling rates is also important for extrapolation to ITER; impurity line radiation in the edge and core of advanced scenarios is guaranteed from the use of edge radiation mantles and the presence of heavy intrinsic or extrinsic non-fully stripped impurities.

5.1. Impurity dependent terms in the modified Rutherford equation

The modified Rutherford equation used for describing the NTM evolution can also provide a convenient framework to study the effect of impurity accumulation and radiation as well as additional cooling at the centre of the island; the time evolution of the width of the island is described by

$$\frac{\tau_{\mathrm{R}}}{r_{\mathrm{s}}}\frac{\mathrm{d}\omega}{\mathrm{d}t} = r_{\mathrm{s}}\Delta' - C_1\left(\frac{\hat{\omega}}{\hat{\omega}^2+\hat{\omega}_\chi^2}\right) + C_2\left(\frac{\hat{\omega}}{\hat{\omega}^2+\hat{\omega}_\chi^2} - \frac{\hat{\omega}_{\Pi}^2}{\hat{\omega}^3}\right) + C_3\hat{\omega} + \frac{C_4}{\hat{\omega}}, \tag{7}$$

where $\hat{\omega} = w/r_{\mathrm{s}}$ and $\hat{t} = t/\tau_{\mathrm{R}}$ are a normalized island size and time and r_{s} is the rational surface location where the TM occurs; $\tau_{\mathrm{R}} = 1.22a^2/(\eta/\mu_0)$ is the 'resistive' time given by the minor radius, plasma resistivity and the magnetic permeability while Δ' is classical tearing stability term. This equation describes the evolution of the full island width including the stabilizing terms due to toroidal geometry ($C_1 = 6D_{\mathrm{R}}$, where

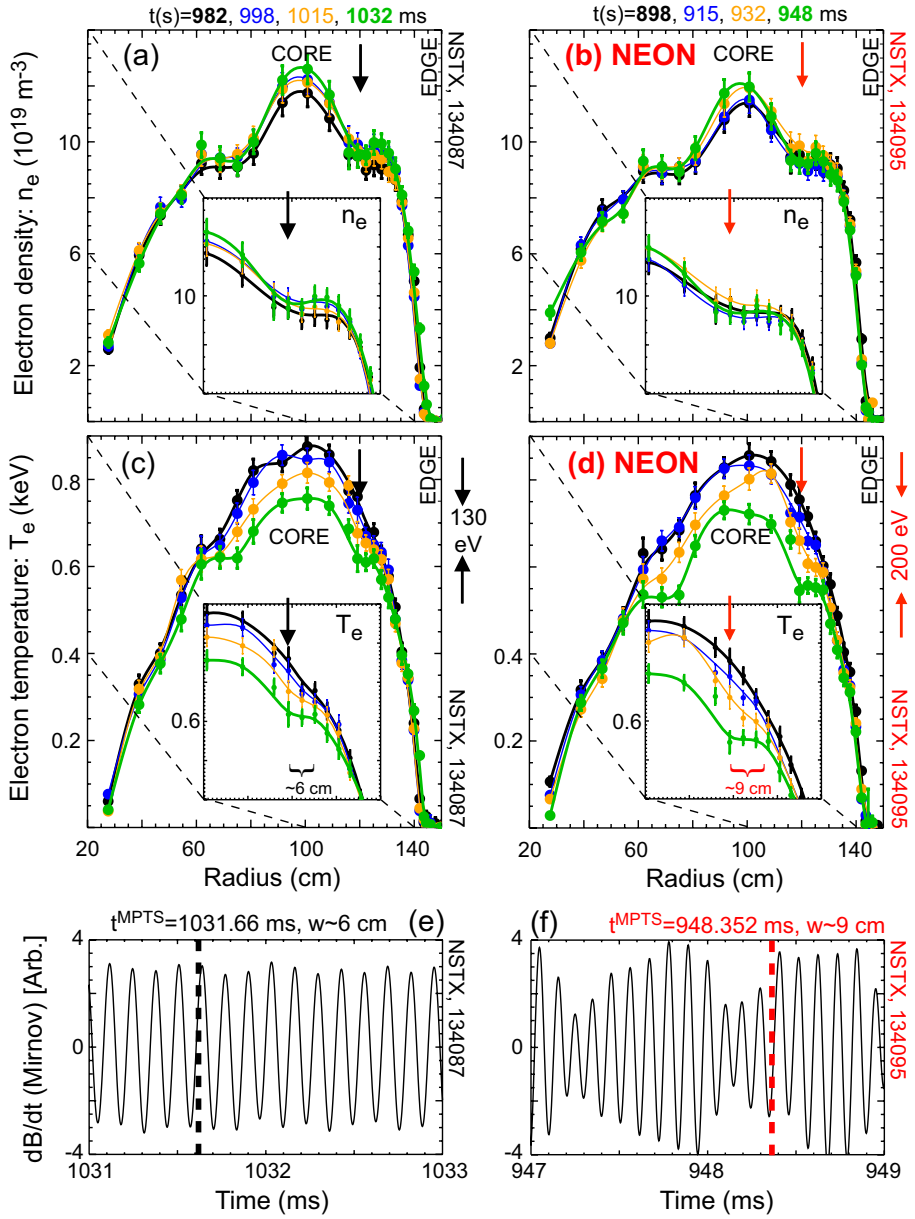

Figure 10. Multi-point Thomson scattering electron (*a*) density and (*b*) temperature data for NSTX shots 134087 and 134095 (neon-seeded). The insets are a 'zoom' of the region of interest where the TM develops. The temperature drops and approximate island size for the neon-free and neon-seeded cases are of the order of 130 versus 200 eV and 6 versus 9 cm, respectively. The MPTS timing for both discharges has the same phase with respect to the island as indicated in (*e*) and (*f*).

$D_R \propto \beta$ is the 'Glasser, Greene and Johnson' term), the neoclassical drive due to the bootstrap current missing inside the island ($C_2 = \sqrt{\frac{r_s}{R}\frac{L_q}{L_p}}\beta_\theta$), and the island width threshold effects (the transport threshold manifested by $\hat{\omega}_\chi = \omega_\chi / r_s$ and the polarization threshold manifested through $\hat{\omega}_\Pi = \omega_\Pi / r_s$) which are important for small TMs. Two additional impurity-dependent terms can be added to the extended MRE: the first one is proportional to the radiated power density within the island and is characterized by the linear dependence between the island growth rate and island size through a dimensionless variable $C_3 = 3(r_s^2/s)\tilde{P}_{rad}/\chi_{\perp,eff}^{island} n_e \langle T_e \rangle$, where $\tilde{P}_{rad} > 0$, $\chi_{\perp,eff}^{island}$, $\langle T_e \rangle$ and $s = (r/q)\,dq/dr = r/L_q$ are the net radiated power density carried by the island, the effective perpendicular thermal conductivity, the average electron temperature in the island and the magnetic shear at the rational surface, respectively. The second term in the extended MRE takes into account the enhancement of impurity density and thus the increase in Z_{eff} at the centre of the island with respect to that of its surroundings through a dimensionless variable $C_4 \approx 5.43 g[s(r_s)]\tilde{Z}_{eff}/Z_{eff}$, where $g[s] = (2-s)/s$ is a function of the magnetic shear [31, 32]. The $\tilde{Z}_{eff}$ term can thus change the sign of $d\omega/dt$ for small islands, even in the presence of a stabilizing Δ', and also contribute, together with the $\tilde{P}_{rad}$ term to the enlargement of the magnetic island. The oversimplified model introduced by Salzedas *et al* [34] can be recuperated from equation (7) by assuming $C_1 = C_2 = C_4 \to 0$; in this case the island growth rate is linearly proportional to the island size and the radiate power density and is sometimes referred to as the radiative-induced tearing

modes (RTMs) description. Previous studies on the onset and evolution of NTMs in NSTX [41–42] have not yet considered the contribution from the P_{rad} and Z_{eff} terms. Verifying the linear scaling law between island growth rate and the island size (ω) including the effect of the radiated power from continuum and line emission ($P_{rad} = P_{Brem} + P_{line}$) is important, as it predicts that an ST-based reactor and even ITER may be susceptible to TM destabilization by impurity radiation. A first order estimate of the total radiated power given by both continuum and line emission and its impact on the 'complete' modified Rutherford equation (including all the terms in the RHS of equation (7)) can be obtained using the cooling rates (L_Z) provided by Post *et al* [43] and will be the subject of future contributions.

5.2. *First NSTX experimental results*

Dedicated experiments have made use of different impurity amounts by extending the neon puff lengths, indicating a relationship between the strength of the radiation emitted, the early appearance of the $m/n = 2/1$ TM as well as the enlargement of the island size; figure 9 depicts the effect that a 10–50 ms Ne-puff have in anticipating the mode onset by 20–80 ms in comparison with that without Ne injection. Both the electron density and temperature profiles before the mode onset and during the island growth for the neon-free and neon-seeded H-modes are also shown in figure 10, and suggest good reproducibility in matching the conditions for the Δ' drive [39]; the insets are a zoom of the region of interest where the TM develops, showing good qualitative agreement with the 'belt-model' described by Chang and Callen [40]. Quantitatively though, the electron temperature drops 130 eV in the neon-free case, indicating also a (mid-plane) saturated island width of approximately 6 cm ($w^* = w/r_s \sim 0.2$, see inset in figure 10(c)), while in the neon-seeded H-mode the electron temperature drop is larger, of the order of 200 eV with the temperature-flattening occurring across a length of ~9 cm ($w^* = w/r_s \sim 0.33$). The comparison of the saturated island widths can be made since the MPTS timing has the same phase with respect to the island as indicated by the Mirnov coil signals shown in figures 10(e) and (f). The change in electron pressure represents the energy loss per unit volume in the electron channel, and thus the estimated power losses (for a $\Delta t \sim 50$ ms) are of approximately ~40 to ~98 mW cm^{-3}. Figure 11 depicts the radiated power density profiles measured by a tangential bolometer for both the neon-free and neon-seeded H-modes; the vertical dotted-line pinpoints the position where the TM develops while the two horizontal lines indicate the first 50 ms from the mode onset (the same time ranges where used in figure 10). The radiated power density losses of 25 and 50 mW cm^{-3} for the same time-range of interest, confirm the apparent relationship between the presence of the enhanced radiation, the strength of the cooling and the enlargement of the saturated island size given by the size of the 'temperature flattening'.

In addition, figure 12 illustrates the low- and high-energy SXR reconstructions for the neon-free and neon-seeded H-modes discussed above. Both the growth of the region with flat low-energy emissivity as well as the decrease in the high-energy emissivity (indicating the plasma cooling at the

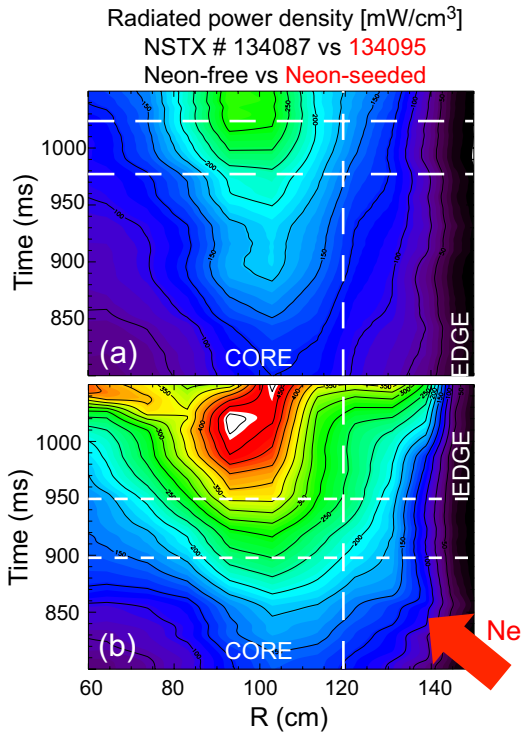

Figure 11. Time history of the radiated power spatial density profiles for the (a) neon-free and (b) neon-seeded H-modes.

island location) are observed at late times ($t > 1000$ ms). The signal-to-noise ratio is considerably better in the case of an impurity seeded plasma and thus is much more obvious from the neon-seeded case that the enhanced radiation from neon continuum and line emission precedes the island formation in the region of interest at mid-radius (see figures 12(c) and (d)). Moreover, the high-energy emissivity also indicates that the plasma cooling at mid-radius took place after the impurity pile-up. Furthermore, the enhancement of the high-energy emissivity seen from figures 12(b) and (d) is of only 25% and accounts for the relative increase in Z_{eff}; the latter is therefore an estimate of how small the increase in resistivity is and thus the effect on the right-hand side of equation (7). However, the enhancement of the low-energy emissivity due to the increased line radiation (P_{line}) is of about 200–300% due to the strong He- and H-like emission; the relative change in line emission strongly dominates over that of the continuum emission (P_{Brems}) and resistivity. In summary, we have found a correlation between the local enhanced neon-radiation, the early appearance of the TM onset at the location where the local radiation is increasing, the enhanced cooling rates as well as the increased island size given by the extension of the temperature-flattening. A quantitative estimate of the impact of both the continuum and line emission on a 'complete' modified Rutherford equation without neglecting the driving and stabilizing terms in equation (7) is a topic of current research in NSTX and will be the subject of future contributions.

6. Summary

Impurity diffusivity levels consistent with the neoclassical predictions have been found, whereas a reversal of the

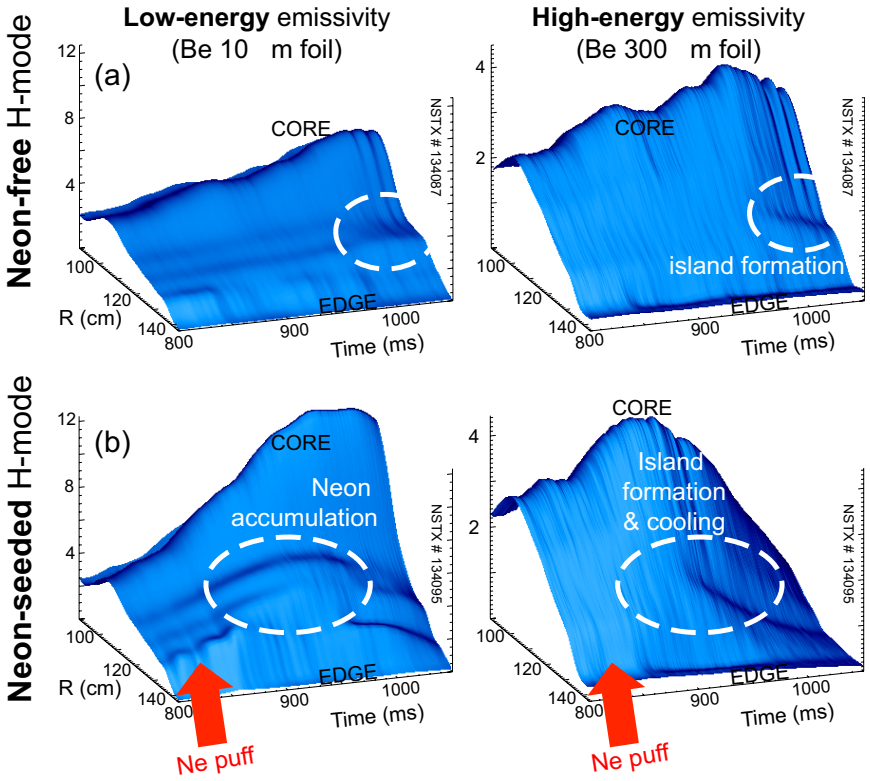

Figure 12. Time history of the low- and high-energy SXR emissivities for both the (*a*) neon-free and (*b*) neon-seeded H-modes.

convective velocity at low fields indicates an anomalous effect to be at play at the gradient region. Different charge state distributions as a consequence of different background plasma parameters have been taken into account when modelling the impurity transport and may be responsible for the change in SXR emissivity in the ν^* scan experiments, but without the need of changing the underlying transport. Studies on the impact of rotation in low-density H-modes (with toroidal rotation velocities of 200–300 km s^{-1}) show that heavy and not fully stripped impurities can experience diffusive and convective coefficients several times larger than that of the standard neoclassical transport for stationary plasmas, without the need of invoking the presence of long wavelength core electrostatic turbulence. As a result of a deliberate neon impurity injection we have also observed a correlation between the strength of the emitted radiation, the earlier appearance of TMs activity and an enhanced plasma cooling that resulted in enlarged magnetic islands.

Acknowledgments

This work was supported by US DoE Contract No DE-AC02-09CH11466 at PPPL and DoE grant No DE-FG02-99ER5452 at Johns Hopkins University. One of the authors (LDA) would like to thank Dr Wayne Houlberg (ITER) for insightful discussions on the role of toroidal rotation on impurity transport.

References

[1] Peng Y.-K.M. *et al* 2005 *Plasma Phys. Control. Fusion* **47** B263
[2] Ono M. *et al* 2000 *Nucl. Fusion* **40** 557
[3] Kotschenreuther M. *et al* 2000 *Nucl. Fusion* **40** 677
[4] Rewoldt G. *et al* 1996 *Phys. Plasmas* **3** 1667
[5] Bourdelle C. *et al* 2003 *Phys. Plasmas* **10** 2881
[6] Delgado-Aparicio L. *et al* 2007 *Appl. Opt.* **46** 6069
[7] Delgado-Aparicio L. *et al* 2007 *J. Appl. Phys.* **102** 073304
[8] Delgado-Aparicio L. 2007 Novel soft x-ray diagnostic techniques for the study of particle transport phenomena in magnetically confined fusion plasmas *PhD Thesis Dissertation* The Johns Hopkins University, USA
[9] Delgado-Aparicio L. *et al* 2007 *Plasma Phys. Control. Fusion* **49** 1245
[10] Delgado-Aparicio L. *et al* 2009 *Nucl. Fusion* **49** 080528
[11] Delgado-Aparicio L. *et al* 2011 *Plasma Phys. Control. Fusion* **53** 035005
[12] Gates D. *et al* 2006 *Phys. Plasmas* **13** 056122
[13] Hulse R. 1983 *Nucl. Technol. Fusion* **3** 259
[14] Stutman D. *et al* 2003 *Phys. Plasmas* **10** 4387
[15] Houlberg W. *et al* 1997 *Phys. Plasmas* **4** 3320
[16] Houlberg W. 2010 International Thermonuclear Experimental Reactor (ITER), private communication
[17] Garbet X. *et al* 2003 *Phys. Rev. Lett.* **91** 035001
[18] Guirlet R. *et al* 2006 *Plasma Phys. Control. Fusion* **48** B63
[19] Angioni C. *et al* 2006 *Phys. Rev. Lett.* **96** 095003
[20] Dubuit N. *et al* 2007 *Phys. Plasmas* **14** 042301
[21] Angioni C. *et al* 2007 *Plasma Phys. Control. Fusion* **49** 2027
[22] Wong K.L. *et al* 1987 *Phys. Rev. Lett.* **59** 2643
[23] Wong K.L. *et al* 1989 *Phys. Fluids* B **1** 545
[24] Romanelli M. *et al* Joint European Torus Report # JET-CP(98)31
[25] Romanelli M. *et al* 1998 *Plasma Phys. Control. Fusion* **40** 1767
[26] Wesson J.A. 1997 *Nucl. Fusion* **37** 577
[27] Suckewer S. *et al* 1984 *Nucl. Fusion* **24** 815
[28] Stutman D. *et al* 2006 *33rd EPS Conf. on Plasma Physics (Rome, Italy, 19–23 June 2006)* vol 30I (ECA) pp P-5.120
[29] Schittenhelm M. *et al* 1997 *Nucl. Fusion* **37** 1255

[30] Oomenes A.A.M. *et al* 2000 *Proc. 18th Int. Conf. on Fusion Energy 2000 (Sorrento, Italy, 2000)* (Vienna: IAEA) CD-ROM file EX/P3-09 and http://www.iaea.org/programmes/ripc/physics/fec2000/html/node1.htm
[31] Pecquet A.-L. *et al* 1997 *Nucl. Fusion* **37** 451
[32] Xiaoming Y.L. 2004 *Plasma Phys. Control. Fusion* **46** 455
[33] Salzedas F. *et al* 2000 *27th EPS Conf. on Controlled Fusion and Plasma Physics (Budapest, 12–16 June 2000)* vol 24B (ECA) pp 25–8
[34] Salzedas F. *et al* 2002 *Phys. Rev. Lett.* **88** 075002
[35] Udintsev V.S. *et al* 2003 *Nucl. Fusion* **43** 1424
[36] Rutherford P.H. 1985 *PPPL Report* 2277
[37] Fredrickson E. *et al* 2000 *Phys. Plasmas* **7** 4112
[38] Fredrickson E. *et al* 2002 *Phys. Plasmas* **9** 548
[39] Chang Z. *et al* 1998 *Phys. Plasmas* **5** 1076
[40] Chang Z. and Callen J.D. 1990 *Nucl. Fusion* **30** 219
[41] Rosenberg A. *et al* 2002 *Phys. Plasmas* **9** 4567
[42] Gerhardt S.P. *et al* 2009 *Nucl. Fusion* **49** 032003
[43] Post D.E. *et al* 1977 *At. Data Nucl. Data Tables* **20** 397